# Perovskite-polymer blends influencing microstructure, non-radiative recombination pathways and photovoltaic performance of perovskite solar cells

Azhar Fakharuddin[*1], Michael Seybold[1], Antonio Agresti[2], Sara Pescetelli[2], Fabio Matteocci[2], Susanne T. Birkhold[1], Hao Hu[1], Rajiv Giridharagopal[4], Iván Mora Seró[3], Aldo Di Carlo[2], Lukas Schmidt-Mende[1]

[1]Department of Physics, University of Konstanz, D-78457, Konstanz, Germany

[2]C.H.O.S.E. Centre for Hybrid and Organic Solar Energy, Department of Electronic Engineering, University of Rome Tor Vergata, via del Politecnico 1, 00133 Rome, Italy

[3]Institute of Advanced Materials (INAM). Universitat Jaume I, 12006 Castelló, Spain

[4]Department of Chemistry, University of Washington, Box 351700, Seattle, Washington 98195-1700, United States

**Abstract**

Solar cells based on organic-inorganic halide perovskite are now leading the photovoltaic technologies due to their high power conversion efficiency. Recently, there have been debates on the microstructure related defects in metal halide perovskites (grain size, grain boundaries, etc.) and a widespread view is that large grains are a prerequisite to suppress non-radiative recombination, and improve photovoltaic performance although opinions against it also exist. Herein, we employ blends of methylammonium lead iodide perovskite with an insulating polymer (polyvinylpyrrolidone, PVP) that offer the possibility to tune the grain size in order to obtain a fundamental understanding of the photoresponse at the microscopic level. We provide, for the first time, spatially-resolved details of the microstructure in such blend systems via Raman mapping, light beam induced current (LBIC) imaging and conductive atomic force microscopy. Although the polymer blend systems systematically alter the morphology by creating small grains (more grain boundaries), they reduce non-radiative recombination

within the film and enhance its spatial homogeneity of radiative recombination. We attribute this to a reduction in the density of bulk trap states, as evidenced by an order of magnitude higher photoluminescence intensity and a significantly higher open-circuit voltage when the polymer is incorporated into the perovskite films. The solar cells employing blend systems also show nearly hysteresis-free power conversion efficiency ~17.8%, as well as a remarkable shelf-life stability over 100 days.

**Introduction**

Organic-inorganic halide perovskite solar cells (PSCs) now demonstrate photovoltaic performance comparable to state-of-the art silicon and thin film solar cells. Their certified power conversion efficiency (PCE, 22.7%),[1] achieved in merely six years since their first high efficiency solid-state cell report in 2012,[2] together with their added functionality such as transparency, flexibility and low temperature compatible roll-to-roll processing put them at forefront of future photovoltaic technologies.[3] After the initial efficiency driven research, the focus nowadays is to understand what makes these devices so well performing and the potential to further improve their photovoltaic (PV) performance. Interfacial engineering to manipulate recombination kinetics at the device interfaces,[4-7] compositional engineering to extend the perovskite absorption region[8] or to enhance its structural stability,[9-10] as well as morphology tuning to obtain a pin-hole free layer or to control non-radiative recombination pathways[11-13] are the key research areas that enabled the remarkable rise in device performance in PSCs.

An important subject in PSCs are their point and structural defect properties that influence band alignment, charge transport/transfer and their stability. These defects – whether present within the bulk, at boundaries between two neighboring grains or at the device

interfaces – are influential to performance and their control is the key to further alleviate the PCE close to its thermodynamic limit.[14] As perovskite films are typically solution-processed at low temperature, a significant density of defects cannot be avoided (~$10^{16}$ $cm^{-3}$).[15-16] Particularly interesting are the defects related to grain boundaries (GBs) as there are reports in favor and against their major role in creating deep trap states. A widespread understanding is that perovskite films comprising large grains (in the range of a few micrometer) are crucial to high performing devices as they contains lesser density of trap states thus leading to lesser non-radiative recombination, enhance light harvesting efficiency and improve charge transport properties.[17-21] Herein, the GBs are considered as a recombination center prevailing non-radiative recombination losses that eventually influence the PV parameters, particularly, the open circuit voltage ($V_{OC}$). This is well explained by Rau using a reciprocity relationship between luminescence properties of solar cells and the $V_{OC}$, showing that $V_{OC}$ could reach its radiative limits ($V_{OC}^{rad}$) if the recombination current at a given voltage is zero.[22]

Recently, significant reduction in non-radiative losses in a mixed halide perovskite ((Cs,MA,FA)$Pb(I_{0.4}Br_{0.6})_3$) based PSCs has been reported when the defects related to GBs are passivated via potassium halide layers.[23] The defect passivation is reflected in the remarkable open circuit voltage ($V_{OC}$) 1.23 V, ~110 mV higher than a reference device employing pristine perovskite without passivation. An enhancement in performance is also noted for metal halide perovskite based LEDs and optical amplifiers by the GBs passivation.[24]

However, contrarily, high charge collection and high performance is also reported using small grains. For example, PCE above 20% is reported in hysteresis-free inverted planar PSCs made using small perovskite grains (100 – 200 nm).[25] Vacuum-based processing of perovskite films results in uniform small crystals that can reach a PCE as high as 20%.[26] Therefore, high-performing PSCs may not always need large grains, and it is rather the nature of GBs that plays

a significant role. This is supported by the findings that the perovskite GBs are benign and only generate shallow in-gap defect states,[27-28] or in some cases are reported to facilitate charge dissociation rather than acting as a recombination center.[29] Chu et al.[30] demonstrated via photoconductivity imaging a spatially homogeneous photoconductivity across the methylammonium lead triiodide films irrespective of the location of GBs, evidencing that the microstructure alone does not significantly influence the photoresponse.

Herein, we employ methylammonium lead triiodide ($MAPbI_3$) perovskite-polymer (Polyvinylpyrrolidone) blend films (hereafter termed as $MAPbI_3$-PVP blend, a method to indirectly tune the morphology (grain size and GBs etc.) and investigate its contribution towards the various optoelectronic and device performance properties. We only employ a small amount of PVP into the $MAPbI_3$ bulk to engineer the morphology and to avoid any significant effect on the conductivity. Such blend systems are reported in PSCs,[31-32] and very recently, making breakthroughs in LEDs,[33-34] however, details on the morphology of the blend systems are rather missing. In this article, we provide details on films morphology via scanning electron microscopy (SEM) and atomic force microscopy (AFM) together with Raman imaging. Light beam induced current (LBIC) and conductive atomic force microscopy (cAFM) imaging allows us to spatially map the microstructure. To the best of our understanding, this is the first report providing spatially resolved characterizations of such systems. We then detail the effect of polymer inclusion in the perovskite bulk by comparing its photoluminescence properties and current-voltage characteristics. Our results show that although polymer additives systematically alter the morphology of perovskite films by creating smaller grain sizes and a higher density of GBs, these blends surprisingly reduce non-radiative recombination within the film.

## Experimental

### Perovskite synthesis and device fabrication

The PSCs were made in glove box following a procedure reported before[35] with some modifications. The precursor solution for the perovskite film consists of methylammonium iodide (MAI), lead iodide ($PbI_2$) and lead chloride ($PbCl_2$) with a molar ratio of 4:1.025:1 in DMF:DMSO (20:1 vol.) resulting in a concentration of 38.8 wt%. The solution was spun on pre-cleaned ITO coated with a PEDOT:PSS layer at 3000 rpm for 20 s. The annealing process is divided into three separate steps. Immediately after spin-coating the films were placed under a vacuum bell and exposed to a pressure of around 2 mbar for 60 s at room temperature to quickly remove excess solvent, followed by a 10 min annealing at 90 °C (at a pressure of ~2 mbar). Finally, the films are annealed at 80 °C for 20 min.

The $MAPbI_3$-PVP blend films are prepared with some modifications: For the precursor solutions, the mass of the MAI and $PbI_2$ was partially substituted by the insulating polymer, PVP. The molecular weight of the used PVP was 55 kDa. Three different concentrations were produced: 0.3 $mg{\cdot}ml^{-1}$, 0.6 $mg{\cdot}ml^{-1}$ and 1 $mg{\cdot}ml^{-1}$. A 15 nm thick $C_{60}$ layer was evaporated to form an electron selective contact, followed by a 1 nm LiF buffer layer. Ag contacts (100 nm) are evaporated to complete the devices at a vacuum of ~$5\times10^{-6}$ mbar.

For high efficiency devices and to enhance the stability of PSCs, oly(3,4-ethylenedioxythiophene) polystyrene (PEDOT:PSS) layer is replaced with a NiO rival. The NiO thin layer was prepared by spin coating Ni(II) acetylacetonate ($C_{10}H_{14}NiO_4$) precursor solution in ethanol (0.5 M) at 5000 rpm and subsequently annealed at 300 – 350 $^{o}$C. For the champion device [6,6]-phenyl-$C_{61}$-butyric acid methyl ester ($C_{60}$) and LiF layers are also replaced with $PC_{60}BM$ (6,6-Phenyl $C_{61}$ butyric acid methyl ester, 99.5%) and Bathocuproine (BCP, 99.99%).

**Morphological, structural and optical characterizations of the blend films**

The film morphology of the $MAPbI_3$-PVP blend systems was studied by scanning electron microscope (Zeiss CrossBeam 1540XB FESEM) equipped with an in-lens detector. The working distance was 5 mm and the acceleration voltage 5 kV was used for imaging. The crystallography of the films was investigated using X-Ray diffraction (Bruker D8 Discover with Lynxeye XE detector, Cu Kα 0.15418 nm). A FluoTime 300 from PicoQuant was used for photoluminescence (PL) spectroscopy. Perovskite films were loaded into a cryostat (Oxford Instruments) and measured under vacuum ($5\times10^{-5}$ mbar). The samples were excited with a 405 nm laser (pulse energy ~3 $\mu j \cdot cm^{-2}$). To get insights into the lifetime, time-resolved PL decays were recorded using time-correlated single photon counting (TCSPC) mode.

The Raman analysis on $MAPbI_3$-PVP samples was carried out by employing a Jobin-Yvon-Horiba micro-Raman system (LabRAM ARAMIS) in a backscattering geometry and by focusing the green laser beam (wavelength $\lambda$ = 514.7 nm) on the perovskite surface. In order to avoid severe laser induced sample degradation occurring during the Raman measurements, we kept the laser power density lower than 26 $W.cm^{-2}$. The spot size was ~1 $\mu m^2$ while a 1800 lines/mm diffraction grating ensured a frequency resolution of about 0.2 $cm^{-1}$. Generally, the Raman signal of the $MAPbI_3$ system presents several limitations[36] such as intrinsic low signal, strong background, complex broad patterns and strong overlapping of the modes with the possible secondary phases (most prominently $PbI_2$). Thus, the acquired raw spectra underwent post-acquisition processing, consisting in subtraction of the fluorescence background performed by a polynomial fitting, while spectral de-convolution was carried out by nonlinear least-squares fitting of the Raman peaks with Gaussian lines shapes.

**Characterization of solar cells and stability measurements**

The light beam induced current (LBIC)[37] was measured by using a chopper that modulates the light at 133 Hz and via two lock-in amplifiers (to enable measurement of low currents limiting the impact of the noise). The light beam is moved across the sample to scan a 1 mm × 1 mm area of the cell. Spatially resolved photocurrent maps were measured by means of an inverted microscope (Leica DMI 5000) coupled with a monochromator (Cornerstone 130) illuminated by a 200 W Xenon Lamp. The wavelength was fixed to 530nm (±2 nm). A long working distance objective with 100x of magnification yielded a 50 µm × 50 µm spot area. The device area was scanned in steps of 25 µm by an x-y motorized stage. The short circuit photocurrents of the devices were measured by a phase sensitive detection system composed by an optical chopper (133 Hz of modulation) and two digital lock-in amplifiers (EG&G 7265).

The current-voltage characteristics of our solar cells (see Figure S1 for the device schematic) were measured in a $N_2$-filled glovebox with a Fraunhofer ISE certified Si reference diode and a KG5 filter, using a Keithley 2410 source meter. For a reliable measurement reporting, we employed a current voltage (*J-V*) measurement tracking algorithm to track the temporal maximum power point (MPP) under illumination as described by Zimmermann et al.[38]

The shelf-life of the PSCs was measured for 100 days. The devices were stored at ambient (room temperature 22±5 $^{o}$C) and at relative humidity that varied between 50 – 70% during the measurement time. For each measurement, only the stabilized PCE value was noted after MPP tracking.

**Results and Discussions**

Figures 1 (a- d) show the morphology of the perovskite films with different polymer concentrations. A clear distinction between the grain size and the nature of GBs is visible

between pristine $MAPbI_3$ film and the $MAPbI_3$-PVP blended films (particularly, 0.6 and 1 $mg.ml^{-1}$ samples). The average grain size calculated from a statistical average (from over 200 grains) is 416 nm for a $MAPbI_3$ film (Figure 1e) whereas upon addition of PVP (0.3 $mg{\cdot}ml^{-1}$) the average grain size decreases to ~230 nm. A further increase in PVP concentration to 0.6 $mg{\cdot}ml^{-1}$ leads to a further reduction in average grain size to 137 nm. For a PVP concentration of 1 $mg{\cdot}ml^{-1}$, the SEM image shows a blurry texture without distinguishable perovskite grains making it impossible to determine a grain size accurately. Nevertheless, a systematic drop in grain size is established via an increasing polymer concentration. We also note an increase in films thickness upon addition of PVP (Figure 1e & Figure S 2, cross-sectional SEM images), which is due to the higher viscosity of the solution due to the long chain polymer, as also reported in literature.[32] Interestingly, we note a reduction in film roughness when the polymer is incorporated in the perovskite films (Figure 1f & SI 3). The root mean square roughness showed a slight drop (from 12.1 for pristine $MAPbI_3$ film to 11.1 for 1 $mg{\cdot}ml^{-1}$ sample) due to the small grains of the blend system.

The crystal structure of the perovskite films on glass is investigated via XRD (Figure 1 g-j). The XRD patterns of all the samples are identical and all the reflexes could be attributed to tetragonal $MAPbI_3$ perovskite.[39] The prominent reflexes of the (110), (220) and (330) lattice planes were found at 14.13°, 28.45° and 43.22°. The broad feature between 15° and 32° is attributed to the amorphous glass substrate underneath the perovskite film. A comparison of pristine perovskite film with those employing polymer shows broadening of the (220) reflex when PVP is included, suggesting a slight reduction in crystallinity upon polymer incorporation which has already shown to reduce the grain sizes. We note an enhanced full width at half maxima of XRD peaks indicating a reduction in crystallite size (calculated using Scherrer equation, see Table S1) that is in good agreement with SEM micrographs.

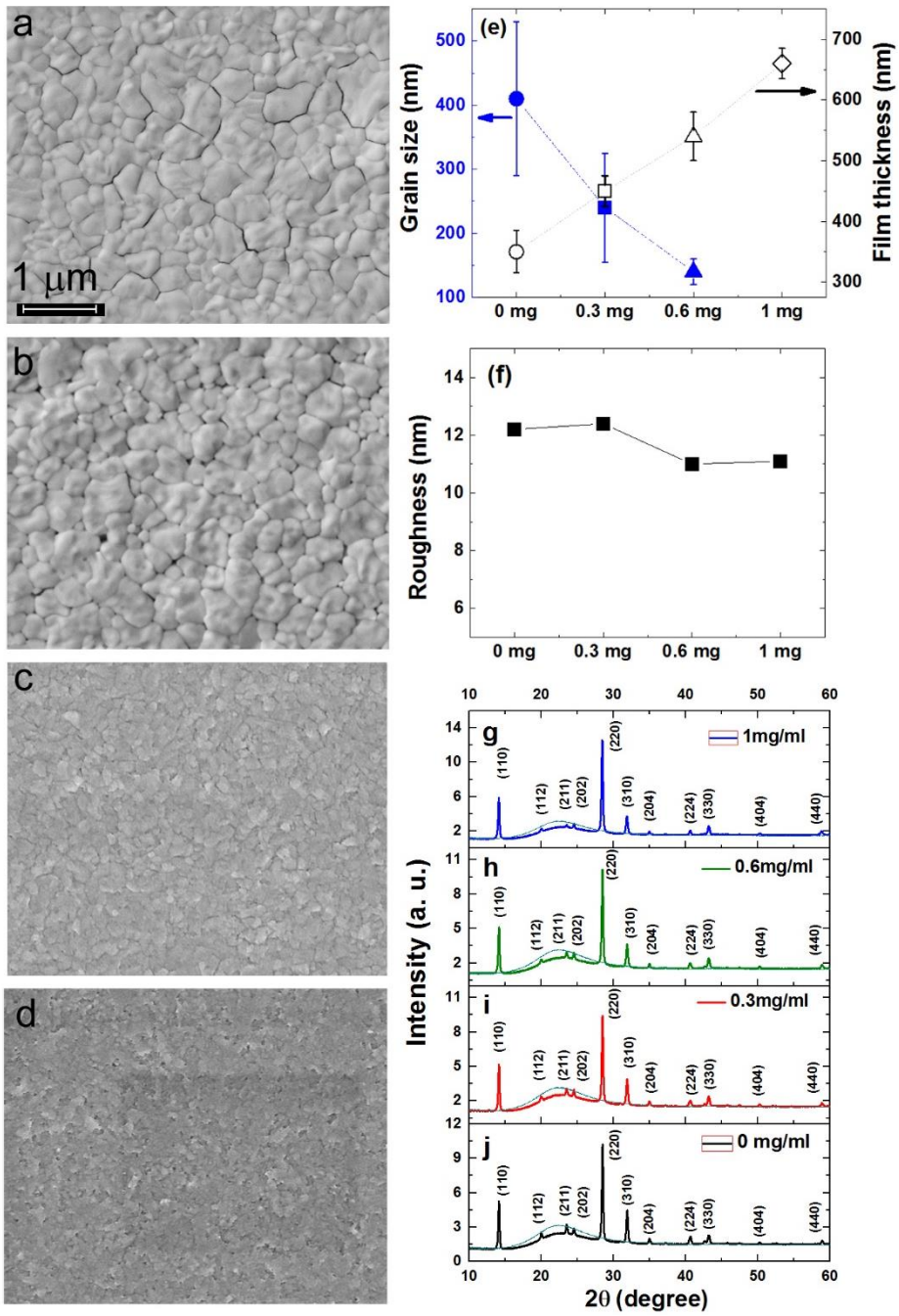


**Figure 1:** SEM images of $MAPbI_3$films with polymer concentrations of (a) 0 mg·ml$^{-1}$, (b) 0.3 mg·ml$^{-1}$, (c) 0.6 mg·ml$^{-1}$ and (d) 1 mg·ml$^{-1}$. Scale bar 1 μm. Figures (e and f) show grain size, film thickness and roughness of all the samples. (g – j) X-ray diffractograms of all the films. The solid lines in the background show XRD of the glass substrate.

In order to probe the radiative/non-radiative recombination and charge extraction, we carried out steady-state photoluminescence (SSPL) measurements of the films deposited on a glass substrate. The emission spectra (Figure 2a) suggests that the PL intensities vary significantly for $MAPbI_3$-PVP blend films; the PL intensity increases with increasing PVP concentration. One

must recall the increase in thickness of perovskite films for PVP based films which may result in a higher light absorption and a higher radiative emission thereby leading to higher PL counts; however, this does not justify the nearly an order of magnitude higher PL emission. We also compare the time-resolved PL (TRPL) decay transients of all perovskite films (Figure 2b) that shows longer carrier lifetime, i.e., the time required for the photogenerated charges to diminish, when the very small amount of PVP in incorporated into the bulk of the $MAPbI_3$ film. The $MAPbI_3$-PVP blend films with the lowest PVP concentration (0.3 $mg{\cdot}ml^{-1}$) showed the shortest decay time, followed by the pristine $MAPbI_3$ and 1 $mg{\cdot}ml^{-1}$ leaving the longest decay time for 0.6 $mg{\cdot}ml^{-1}$. A comparison of the two distinct regions in the PL decay transient, the initial fast (attributed to a trap-assisted non-radiative decay) and the slow (attributed to radiative recombination of the free charge carriers),[40] suggests a lower trap density for the $MAPbI_3$-PVP blend films, the lowest for 0.6 $mg{\cdot}ml^{-1}$. The pristine $MAPbI_3$ films show a fast initial decay followed by a slow long tail whereas the $MAPbI_3$-PVP blend films (particularly with higher PVP concentration).

We note the discrepancy between SSPL and TRPL for the 0.6 and 1 $mg{\cdot}ml^{-1}$ samples. We emphasize that term carrier lifetime is rather poorly defined as suggested by Tress[41] and it should be carefully interpreted when referring to a longer (shorter) lifetime. Tress explained that a shorter radiative lifetime is not detrimental and it rather the competition between radiative (RR) and non-radiative recombination (NRR) that matters (ideally the NRR should be as long as possible leading to high radiative yield). This is the case for most efficient perovskite based LEDs in literature. Another important consideration is that the SSPL only provides information on the total RR (at a given time only), whereas the TRPL depicts relaxation behavior of the initial photogenerated charge carrier density (which is a superimposition of both the RR and NRR).[42] It should be noted that while the TRPL measures only the charges

recombining radiatively on a purely time-dependent scale, the shape of the transient is dominated by non-radiative recombination, the initial fast decay being assigned to charge trapping whereas the longer tail could be dominated by a slower charge relaxation (probably from the shallowly trapped charges being emitted, reabsorbed and re-emitted). The latter is particularly the case when the slower decay component of TRPL is non-linear and accompanied by a drop in PL intensity (evidencing a reduction in RR). However, when a slower (longer) lifetime accompanied by an increase in the PL intensity is an indication of the dominant RR. Since the TRPL spectrum is typically plotted on a normalized scale, the total PL intensity (as measured in SSPL) should not be anticipated as an indication of longer carrier diminishing time.[43] Whereas, the initial fast decay in the TRPL spectra is dominated by trap-assisted recombination, the slower long tail could also arise delayed PL from the shallowly trapped charges.[44] Taking these considerations into account, we suggest that the difference between the slower decay for 0.6 and 1 mg·ml$^{-1}$ samples should be understood as the different trap density of the two films, being more dominant for the 0.6 mg samples, as also evident from the its lower PL intensity in SSPL (Figure 2a).

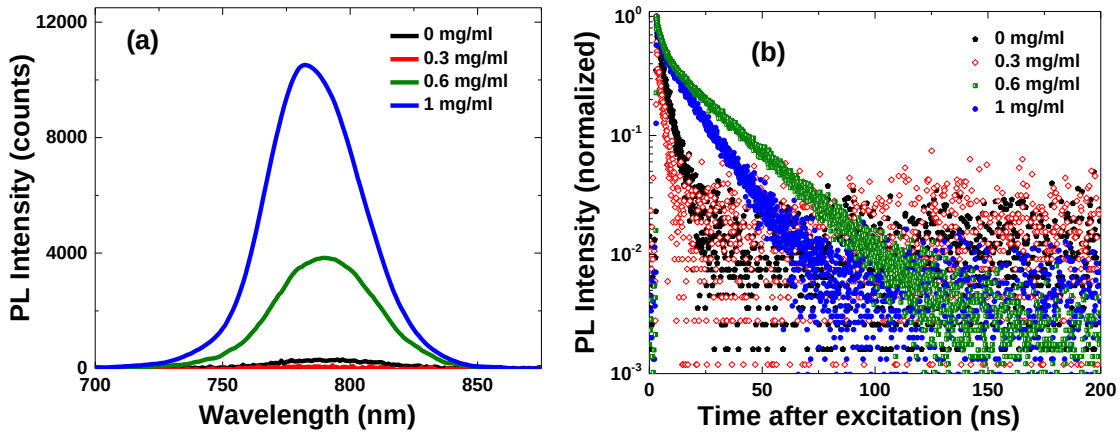


**Figure 2:** (a) PL emission spectra of $MAPbI_3$ films with PVP concentrations of 0, 0.3, 0.6, and 1 mg·ml$^{-1}$ and (b) PL decay transients of the same measured at excitation wavelength 405 nm, and laser fluence 3.07 µJ·cm-2. For both measurements, the $MAPbI_3$ films (on glass) were excited from the perovskite side.

The remarkable increase in PL intensity for $MAPbI_3$-PVP blends (despite the similar absorbance, see Figure S 4), particularly, the 0.6 and 1 $mg \cdot ml^{-1}$ samples, suggests a significant reduction in non-radiative recombination pathways, possibly due to a reduction in structural defects and/or grain boundary passivation. The $MAPbI_3$-PVP blend films show different morphology than a pristine rival, with larger number of small grains and more GBs. Important to note is the difference in the nature of the GBs between the two samples: Whereas the pristine $MAPbI_3$ film shows large grains with deep GBs, the $MAPbI_3$-PVP blend films show smaller inter-diffused grains, probably passivated by the PVP. This suggests that large grains may not necessarily guarantee a lower trap state density in the perovskite film and it is rather the nature of GBs (vertical/lateral, depth etc.) that also influences the defect properties. We also compared steady-state PL and PL decays of all the perovskite films excited through front (film side) and back side (glass side) of the films (Figure S 5), affirming the reduction of trap states density and longer carrier lifetime with increasing PVP concentration. In addition, a comparison of time dependant tracking of PL intensity of a $MAPbI_3$ film and the highest PVP concentration under continuous laser exposure (a method used to demonstrate trap-filling in literature)[45] further affirmed reduction in trap density in the blend system (Figure S 6).

In order to investigate any structural changes in the $MAPbI_3$-PVP blend systems, we performed a Raman analysis of the films. Prior to obtaining Raman maps, we record optical images of all the $MAPbI_3$ films. Notable is the difference in the morphology of the films depending on the PVP concentration (Figure 3a & Figure S 7). The highest PVP concentration (1 $mg \cdot ml^{-1}$) showed darker extended domains unlike a homogeneous film texture in a pristine $MAPbI_3$ film. We, however, cannot rule out a contribution due to the height difference in the films that may leads to contrast in the images. In order to confirm whether the difference in the contrast arises from height difference or a different $MAPbI_3$-PVP ratio, we recorded Raman spectra of

a pristine $MAPbI_3$ film and compared it with the spectra taken at a dark and faded region of the 1 mg·ml$^{-1}$ sample (Figure 3 b).

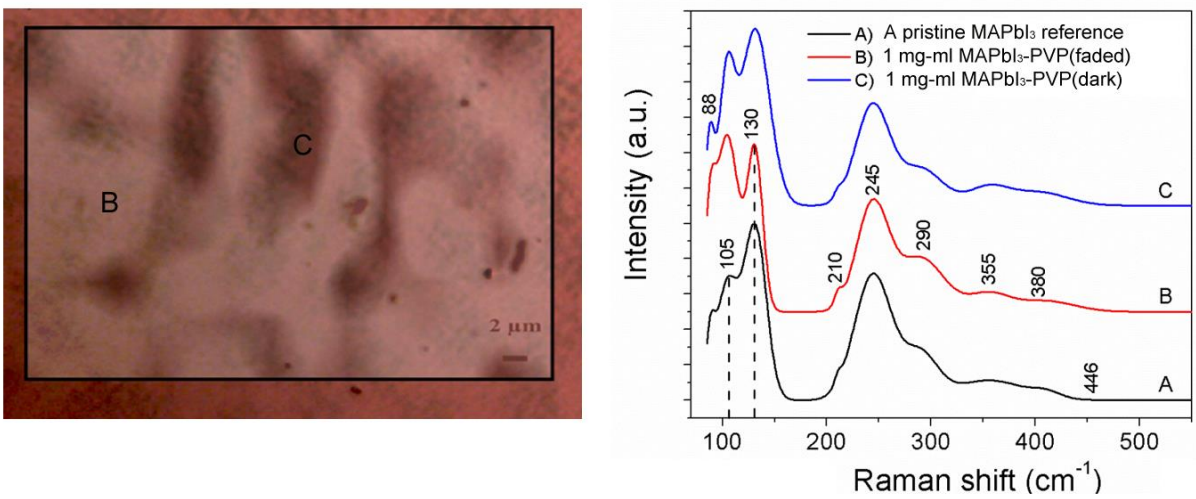


**Figure 3:** (left) Superimposition of scanned area optical image and 130 cm$^{-1}$ Raman band intensity map of a $MAPbI_3$-PVP blend sample (1 mg.ml$^{-1}$) taken from 50X ultra long working distance objective, and (rights) Raman spectra acquired on $MAPbI_3$ films without (curve A) and with PVP (1 mg.ml$^{-1}$) at two different regions acquired by focusing the laser beam on faded and dark areas respectively, as indicated in the optical images (curve B and C, respectively).

All the reported spectra showed the typical $MAPbI_3$ vibrational modes, in agreement with recently published Raman investigation on perovskite layers.[36] In particular, at lower wavenumbers, three main vibrational modes are evident (89, 105, and 130 cm$^{-1}$) while the higher wavenumbers spectral region is dominated by the peak at 245 cm$^{-1}$ and five less intense contributions (210, 290, 355, 380, and 446 cm$^{-1}$). We cannot distinguish any PVP Raman band in all the $MAPbI_3$-PVP blend films, probably due to the low polymer concentration used in the perovskite precursor solution. Theoretical calculations of the MAPI vibrational modes assigned the 89 and 105 cm$^{-1}$ peaks to the vibrations of the Pb-I cage while the broadest band at 245 cm$^{-1}$ to the MA cation torsional modes.[46] Differently from the spectra reported in literature, we observed a prominent peak at 130 cm$^{-1}$ that could be a superimposition between the two peaks usually observed at 122 cm$^{-1}$ and at 138cm$^{-1}$ ascribed to the Pb-I cage vibration[47] and to the liberation of the organic cation respectively.[36] Moreover, we can confidently exclude a laser induced film degradation since the typical peaks of $PbI_2$ at 96 cm$^{-1}$

and 113 $cm^{-1}$ are not present in the acquired spectra. Notably, the relative intensity between the two adjacent peaks at 105 and 130 $cm^{-1}$ changes when polymer is added to the perovskite precursor and increases in the dark area of perovskite film with 1 $mg{\cdot}ml^{-1}$ PVP. The other Raman bands are not significantly affected by the presence of the polymer. As changes in the 130 $cm^{-1}$ peak correlate with the presence of the polymer in $MAPbI_3$-PVP blend films, we decided to characterize spatial homogeneity/distribution of the PVP in the bulk of the perovskite.

Figure 4 (a – d) displays the 130 $cm^{-1}$ Raman band intensity maps of all the samples showing that the areas with higher intensity increases with the amount of PVP. In fact, the intensity distribution of the 130 $cm^{-1}$ Raman band could be correlated with their morphology (Figure S7) by superimposing them on top of their optical images (Figure S8). As depicted in Figure S 8, the darker area corresponds to the most intense Raman signal at 130 $cm^{-1}$, thereby highlighting the role of PVP in creating domains with different Raman features. From these considerations, we are able to chemically map the film morphology by evaluating the domains size depending on the PVP concentration. We note that the domains are elongated in shape and larger in size when a higher PVP concentration is used, while in the case of 0.3 $mg{\cdot}ml^{-1}$ are spotted shaped with an average diameter of about 5-10 µm. One should note that Raman mapping superimposed with optical images only provide details at the micrometer level and may not be correlated with SEM images with nanometer resolution.

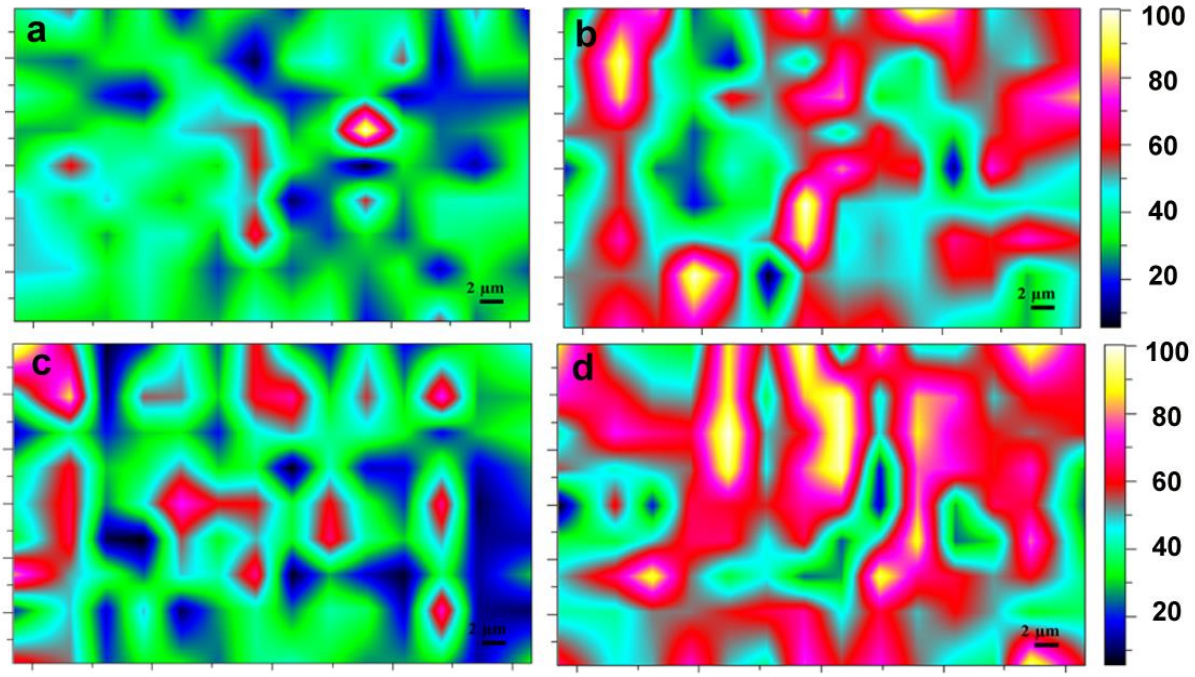


**Figure 4**: Mapping of the intensity of 130 $cm^{-1}$ Raman band all investigated perovskite film a) reference film without PVP, b) 0.3 $mg.ml^{-1}$, c) 0.6 $mg.ml^{-1}$ and d) 1 $mg.ml^{-1}$. The scale bar is 2 µm.

In order to further investigate the spatial PVP distribution within the perovskite films, the lateral current distribution was studied using LBIC. Figure 5 (a – d) shows the local current mapping over an area of 1 × 1 $mm^2$. The reference device (without PVP) shows a spatial homogeneous current in the range of 52 - 55 nA. Surprisingly, the addition of PVP led to a notable increment in the local current; the current raises to 62 - 67 nA for 0.3 $mg{\cdot}ml^{-1}$ and 0.6 $mg{\cdot}ml^{-1}$ based devices, although few spots with reduced current (45 - 55 nA) are also visible. The low current spots are between 0.05 mm and 0.1 mm which could be attributed to intermixed $MAPbI_3$-PVP phases. Those local patches of reduced current are even more pronounced at 1 $mg{\cdot}ml^{-1}$ PVP concentration, stretching over several hundred microns. However, we note that PVP does not form agglomerates but is rather disperses in the $MAPbI_3$ films, as in the case of PVP agglomerates, completely insulating domains should have been formed contributing to regions with no current. LBIC measurements (Figure 5) suggest that the obtained spatial photocurrent is slightly higher when PVP is added to the perovskite.

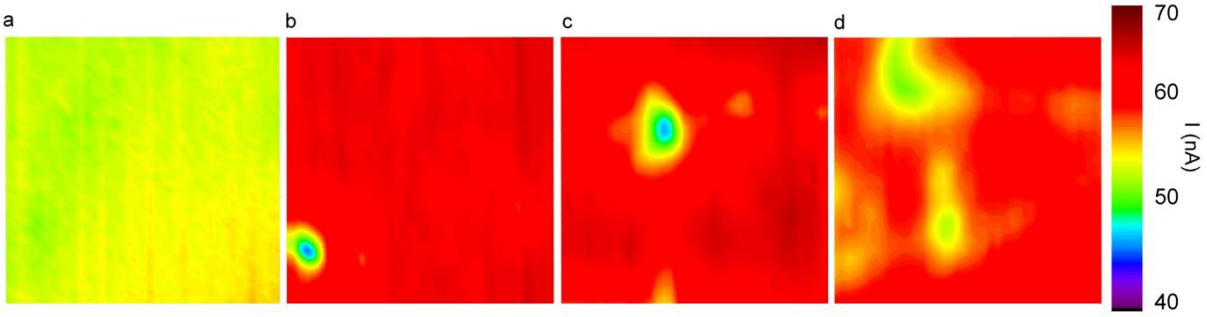


**Figure 5 (a – d):** Light Beam Induced Current (LBIC) measurements of the perovskite solar cells with (a) 0, (b) 0.3 (c) 0.6, and (d) 1 mg·ml$^{-1}$ PVP concentration. The dimensions are 1 × 1 mm$^2$.

To further investigate spatial conductivity of the films, we recorded cAFM maps of samples with much higher polymer concentrations. We intentionally prepared samples with a higher PVP concentration in order to trace the PVP in $MAPbI_3$ films, and to see if it forms any insulating patches. The images of samples with much higher PVP concentration (5 and 10 mg·ml$^{-1}$) further confirm that PVP does not form large insulating patches (Figure S 9) and the conductivity is homogeneously distributed across the film, even at a nanometre scale. This proves that no insulating areas are formed upon incorporation of polymer.

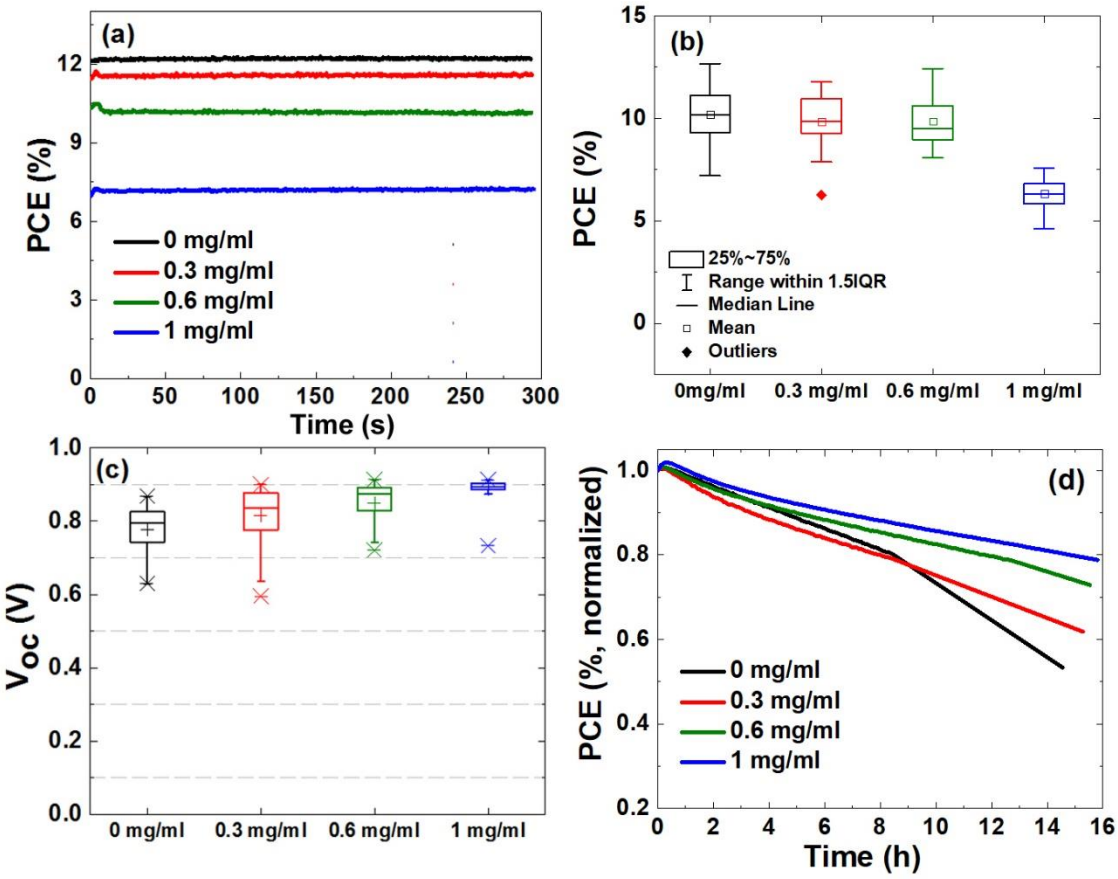


**Figure 6:** (a) Maximum power point (MPP) tracking of the PSCs made with different PVP concentrations (ITO/PEDOT:PSS/$MAPBbI_3$/$C_{60}$LiF/Ag) measured at 82 mW.cm$^{-2}$. (b) A statistical analysis of PCE of at least 20 devices, (c) and open circuit voltage (c) of all the PSCs. (d) The PCE of all the PSCs measured in $N_2$ atmosphere under continuous light soaking (82 mW.cm$^{-2}$).

In order to accurately compare the photovoltaic performance of PSCs made using different concentration of polymer, we carried out a MPP tracking protocol as suggested by Zimmermann et al.[38] Figure 6a displays the PCE of the champion device using PEDOT:PSS as a hole transport layer while 6b shows the average PCE made from at least 20 selected solar cells. The PCE showed little increase in the beginning but it stabilizes quickly and remained stable during the rest of the tracked time. We note that the average PCE of the lower concentrations of PVP (0.3 and 0.6 mg·ml$^{-1}$) remains almost similar to a reference cell employing pristine $MAPbI_3$ film (10 – 12%), whereas, for the highest PVP concentration, the PCE shows a significant drop. The J-V curves of the champion devices and a statistical analysis of J-V

parameters of all the devices are shown in Figure S 10. We also note a slight increase in hysteresis index for higher polymer concentrations (Figure S 11).

Noteworthy is the improvement in the open circuit voltage ($V_{OC}$) of the PSCs upon PVP inclusion. Figure 6c depicts an average $V_{OC}$ of at least 20 PSCs of each type. The mean $V_{OC}$ increases from 0.78 V for the reference cell (0 mg·ml$^{-1}$) to 0.82 V, 0.85 V, 0.9 V for 0.3, 0.6 and 1 mg·ml$^{-1}$ PVP concentration sample, respectively. The increase of $V_{OC}$ is in good agreement with the decrease of non-radiative recombination observed by PL measurements, see Figure 2. The change in the $V_{OC}$ suggests a variation in the competition between radiative and non-radiative recombination arising from improvement in the bulk defects (morphological, structural and point defects) upon polymer incorporation.

In order to compare the stability of the various devices, we carried out light soaking of the PSCs in glove box under continuous solar irradiation (82 mW.cm$^{-2}$) for >15 h. The MPP of the devices were tracked and a J-V measurement was taken periodically every 10 minutes (Figure 6d). Whereas the reference cell dropped by 70% of its initial PCE after 15 h, the devices with higher concentration of PVP (0.6 and 1 mg.ml$^{-1}$) showed a smaller drop (26% and 21%, respectively) in the initial PCE. The 0.3 mg.ml$^{-1}$ sample showed a faster initial degradation, however, after 5 h the degradation was slower than for the reference device. The effect of light soaking on other PV parameters such as $J_{SC}$, $V_{OC}$, and the fill factor (FF) is shown in Figure S 12.

While PEDOT:PSS is a standardized material convenient for the preparation of benchmark samples, PSCs based on PEDOT:PSS typically yield a lower PV performance for inverted perovskite solar cells, and also have a poor stability due to its corrosive nature to ITO.[4] For a further optimization, we replaced it with a solution-processed NiO compact layer. To compare with a reference NiO device (employing pristine $MAPbI_3$), we only highlight 0.6 mg.ml$^{-1}$ PVP

concentration as it showed a compromise over PCE and stability and recorded its PV performance and stability. The stabilized J-V curves of all the PSCs (measured at 1 sun) are shown in Figure 7a. Whereas the PEDOT:PSS based devices showed a PCE 12.03 % (forward scan 11.97%, reverse scan 12.09%), the reference device employing NiO layer showed a remarkable improvement in PV parameters. A remarkable improvement in the $V_{OC}$ and $J_{SC}$ yielded PCE 17.48% (forward scan 17.02%, reverse scan 17.48%). Interestingly, the 0.6 $mg.ml^{-1}$ PVP based PSCs showed slightly higher PCE (17.78%), primarily due to the higher $V_{OC}$ ~1.11 V (forward scan 17.70%, reverse scan 17.87%) that is in good agreement with the trend observed for PEDOT:PSS. We note that these values employing NiO as HTL are amongst the highest reported so far. Notably, the PVP based devices showed slightly higher hysteresis index and slight drop in fill factor compared to the reference NiO based PSC (see details of J-V parameters in Table S2). The higher $V_{OC}$ in the PSCs made using the blend system affirms a reduction in bulk defects, which act as a recombination center. This high performance in PSCs employing blend systems, despite larger number of GBs is remarkable. It confirms that the number of GBs alone may not contribute to defects density (and non-radiative recombination) but the nature of GBs is more crucial. In the case of pristine $MAPbI_3$ films (with no polymer inside), although large grains are visible (SEM images, Figure 1), a clear deep grain boundary between neighboring grains is distinguishable. Whereas in the case of the blend system, a highly homogeneous microstructure is observed.

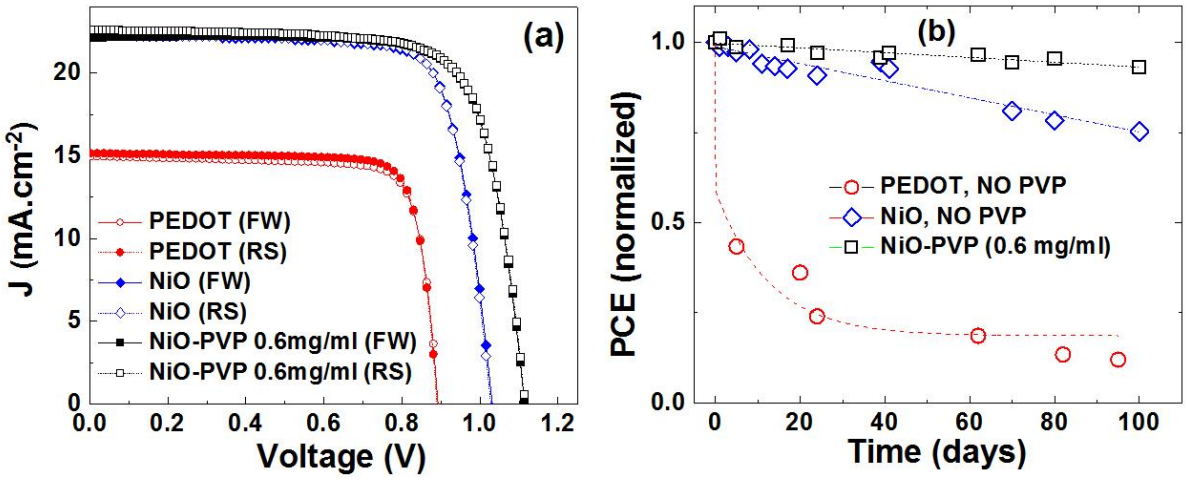


**Figure 7:** (a) Stabilized current-voltage curves of PSCs labelled as PEDOT (PEDOT:PSS/$MAPbI_3$/$PC_{60}BM$/BCP/Au), NiO (NiO/$MAPbI_3$/$PC_{60}BM$/BCP/Au) and NiO-PVP 0.6 mg (NiO /$MAPbI_3$-PVP/$PC_{60}BM$/BCP/Au), measured in ambient at 1 sun. (b) Shelf-life performance of representative devices of each type, stored at ambient and at relative humidity between 50 – 70%.

Finally, in order to compare the shelf-life of the various PSCs, we carried out their shelf-life stability testing. The cells were stored in dark in ambient and measured at room temperature at a relative humidity between 50 – 70%. The PSCs employing PEDOT:PSS layer showed a ~ 80% drop in the initial PCE in merely 20 days, whereas the PCE of a reference cell made using NiO (without PVP) dropped only by 25% after 100 days. These results highlight the importance of choosing selective contacts towards long-term stability of the performance.[4] Interestingly, the PSCs made using blend system retained >92% of the initial PCE at similar experimental conditions. Despite the smaller grain size in these devices, their stable performance compared to a NiO reference rival (with large perovskite grains) is remarkable.

Our results suggest high performance can also be obtained using small $MAPbI_3$ grains. The pursuit of large grains is because of the understanding that the grain boundary is a recombination center where dangling bonds form deep levels within the band gap resulting in charge traps. However, an efficient passivation can reduce the deleterious effect[24]. At the same time such passivation can also effect positively the device lifetime. Therefore grain boundaries need to be reconsidered, as it was recently even shown that GBs are not always

undesirable.[29-30] For example, Yun et al. demonstrated that GBs are in fact beneficial for charge separation and collection.[48] Similarly, recently shown highest performance (>20%) in planar PSCs employ perovskite films made of small grains.[25] Our results further confirm these latest trends in PSCs.

**Conclusions**

In conclusion, we provide a systematic investigation of the role of the grain size and grain boundary towards recombination, photovoltaic performance and stability of perovskite solar cells by employing $MAPbI_3$-PVP blend systems. Interestingly we note that the $MAPbI_3$-PVP blend films featuring small sized grains show reduced non-radiative recombination compared to their pristine $MAPbI_3$ rivals. The light beam induced current (LBIC) mapping of the devices measuring photoresponse down to microscopic level shows a higher local current in films employing small grains, corroborating the trends of the photoluminescence transient decay curves. This is in accordance with few recent reports in literature that grain boundaries in halide perovskite are in fact benign and favor charge dissociation and that high efficiency devices do not necessarily require large grains.

In addition, we also, for the first time, provide spatially resolved insights into the morphology of such blend systems via Raman mapping, LBIC and conducting atomic force microscopy. These spatially resolved techniques lead us to conclude that the polymer disperses in the bulk of the $MAPbI_3$ film and also that it does not form agglomerates nor does it remain on the surface (which would otherwise hinder charge collection). Interestingly, we note that although the addition of low concentrations of an insulating polymer creates small grains (more GBs), it also reduces non-radiative recombination within the film which we attribute to the reduction in the density of bulk by the polymer passivation. We further support our arguments

of the reduction of the trap states by an order of magnitude higher photoluminescence yield and a remarkable open-circuit voltage (1.11 V) in the $MAPbI_3$-PVP blend films, ~80 mV higher than a device employing pristine $MAPbI_3$ film. Finally, we also show that the solar cells employing $MAPbI_3$-PVP blend films demonstrate a stabilized nearly hysteresis-free power conversion efficiency of ~17.8% and significantly enhance the long term stability. Our results pave the way for further enhancement of stability without affecting the solar cell performance.

**Supporting Information**

The Supporting Information is available free of charge on the ACS Publications website at DOI….

Schematic of solar cell architecture, cross sectional SEM of perovskite films, AFM topography of the various perovskite films, absorbance and emission spectra, steady-state and time resolved photoluminescence spectra of the various perovskite films excited through film and glass side as well as a time dependent-PL intensity tracking, superimposition of optical image and Raman mapping of the perovskite films, cAFM images showing local conductivity, current-voltage characteristics curves, statistics and hysteresis index of solar cells, continuous light soaking test results, and J-V parameters of the champion devices.

**Author information**

*Email: azhar-fakhar.uddin@uni-konstanz.de (A. F.)

**ORCID**

Azhar Fakharuddin: 0000-0001-5589-4265
Antonio Agresti: 0000-0001-6581-0387
Sara Pescetelli: 0000-0002-3336-2425.
Fabio Matteocci: 0000-0001-7893-1356
Susanne T. Birkhold: 0000-0003-1364-9944
Rajiv Giridharagopal: 0000-0001-6076-852X
Iván Mora Seró: 0000-0003-2508-0994
Aldo Di Carlo: 0000-0001-6828-2380
Lukas Schmidt-Mende: 0000-0001-6867-443X

**Authors' contribution**

A.F. and M.S. carried out most of the experimental work. H.H. and S.B. assisted in device fabrication. F.M., A.A, S.P. and A.D.C. carried out LBIC and Raman mapping. R. G. was responsible for conducting c-AFM. IMS and LSM involved in discussions on data analysis. A.F. prepared the manuscript and all authors took part in discussion and correction.

**Acknowledgement**

A.F. acknowledges financial support from Alexander von Humboldt and A.F. and L.S.M. from the ERANET project Hydrosol. S.T.B acknowledges financial support from the Carl Zeiss Foundation. We thank David S. Ginger (University of Washington) for use of AFM facilities for cAFM measurements. R.G. acknowledges support from DOE (DE-SC0013957).

## References


(1) NERL, Best research cell efficiencies (2018). NREL, Ed. 2018.

(2) Lee, M. M.; Teuscher, J.; Miyasaka, T.; Murakami, T. N.; Snaith, H. J. Efficient hybrid solar cells based on meso-superstructured organometal halide perovskites. *Science* **2012,** *338* (6107), 643-647, DOI: 10.1126/science.1228604.

(3) Di Giacomo, F.; Fakharuddin, A.; Jose, R.; Brown, T. M. Progress, challenges and perspectives in flexible perovskite solar cells. *Energ. Environ. Sci.* **2016,** *9* (10), 3007-3035.

(4) Fakharuddin, A.; Schmidt-Mende, L.; Garcia-Belmonte, G.; Jose, R.; Mora-Sero, I. Interfaces in Perovskite Solar Cells. *Advanced Energy Materials* **2017,** *7* (22), 1700623, DOI: doi:10.1002/aenm.201700623.

(5) Wong, K. K.; Fakharuddin, A.; Ehrenreich, P.; Deckert, T.; Abdi-Jalebi, M.; Friend, R. H.; Schmidt-Mende, L. Interface-Dependent Radiative and Nonradiative Recombination in Perovskite Solar Cells. *The Journal of Physical Chemistry C* **2018,** *122* (20), 10691-10698, DOI: 10.1021/acs.jpcc.8b00998.

(6) Agresti, A.; Pescetelli, S.; Cinà, L.; Konios, D.; Kakavelakis, G.; Kymakis, E.; Di Carlo, A. Efficiency and Stability Enhancement in Perovskite Solar Cells by Inserting Lithium-Neutralized Graphene Oxide as Electron Transporting Layer. *Advanced Functional Materials* **2016,** *26* (16), 2686-2694, DOI: doi:10.1002/adfm.201504949.

(7) Palma, A. L.; Cinà, L.; Pescetelli, S.; Agresti, A.; Raggio, M.; Paolesse, R.; Bonaccorso, F.; Di Carlo, A. Reduced graphene oxide as efficient and stable hole transporting material in mesoscopic perovskite solar cells. *Nano Energy* **2016,** *22*, 349-360, DOI: https://doi.org/10.1016/j.nanoen.2016.02.027.

(8) Jeon, N. J.; Noh, J. H.; Yang, W. S.; Kim, Y. C.; Ryu, S.; Seo, J.; Seok, S. I. Compositional engineering of perovskite materials for high-performance solar cells. *Nature* **2015,** *517* (7535), 476-480, DOI: 10.1038/nature14133.

(9) Saliba, M.; Matsui, T.; Seo, J.-Y.; Domanski, K.; Correa-Baena, J.-P.; Nazeeruddin, M. K.; Zakeeruddin, S. M.; Tress, W.; Abate, A.; Hagfeldt, A.; Gratzel, M. Cesium-containing triple cation perovskite solar cells: improved stability, reproducibility and high efficiency. *Energ. Environ. Sci.* **2016**, DOI: 10.1039/C5EE03874J.

(10) Leijtens, T.; Eperon, G. E.; Noel, N. K.; Habisreutinger, S. N.; Petrozza, A.; Snaith, H. J. Stability of metal halide perovskite solar cells. *Advanced Energy Materials* **2015,** *5* (20), DOI: 10.1002/aenm.201500963.

(11) Li, G.; Ching, K. L.; Ho, J. Y. L.; Wong, M.; Kwok, H.-S. Identifying the Optimum Morphology in High-Performance Perovskite Solar Cells. *Advanced Energy Materials* **2015**, n/a-n/a, DOI: 10.1002/aenm.201401775.

(12) Matsumoto, F.; Vorpahl, S. M.; Banks, J. Q.; Sengupta, E.; Ginger, D. S. Photodecomposition and Morphology Evolution of Organometal Halide Perovskite Solar Cells. *Journal of Physical Chemistry C* **2015,** *119* (36), 20810-20816, DOI: 10.1021/acs.jpcc.5b06269.

(13) Wu, Y.; Chen, W.; Yue, Y.; Liu, J.; Bi, E.; Yang, X.; Islam, A.; Han, L. Consecutive Morphology Controlling Operations for Highly Reproducible Mesostructured Perovskite Solar Cells. *ACS Applied Materials and Interfaces* **2015,** *7* (37), 20707-20713, DOI: 10.1021/acsami.5b05576.

(14) Ball, J. M.; Petrozza, A. Defects in perovskite-halides and their effects in solar cells. *Nature Energy* **2016,** *1*, 16149, DOI: 10.1038/nenergy.2016.149.

(15) Wenger, B.; Nayak, P. K.; Wen, X.; Kesava, S. V.; Noel, N. K.; Snaith, H. J. Consolidation of the optoelectronic properties of CH3NH3PbBr3 perovskite single crystals. *Nature Communications* **2017,** *8* (1), 590, DOI: 10.1038/s41467-017-00567-8.

(16) Giovanni, L.; Christoph, N. H.; Carlo, B.; Costantino, M.; Felix, L.; Steve, A.; Bernd, R.; Sergio, P. Correlation between Electronic Defect States Distribution and Device Performance of Perovskite Solar Cells. *Advanced Science* **2017,** *4* (10), 1700183, DOI: doi:10.1002/advs.201700183.

(17) Chen, J.; Shi, T.; Li, X.; Zhou, B.; Cao, H.; Wang, Y. Origin of the high performance of perovskite solar cells with large grains. *Applied Physics Letters* **2016,** *108* (5), 053302, DOI: 10.1063/1.4941238.

(18) Mingzhu, L.; Tiankai, Z.; Wangying, X.; Xiaoliang, Z.; Fangyan, X.; Qiang, L.; Zefeng, C.; Fengrui, Z.; Sing, W. K.; Keyou, Y.; Jianbin, X. Large-Grain Formamidinium PbI3–xBrx for High-Performance Perovskite Solar Cells via Intermediate Halide Exchange. *Advanced Energy Materials* **2017,** *7* (12), 1601882, DOI: doi:10.1002/aenm.201601882.

(19) Trilok, S.; Tsutomu, M. Stabilizing the Efficiency Beyond 20% with a Mixed Cation Perovskite Solar Cell Fabricated in Ambient Air under Controlled Humidity. *Advanced Energy Materials* **2018,** *8* (3), 1700677, DOI: doi:10.1002/aenm.201700677.

(20) He, M.; Li, B.; Cui, X.; Jiang, B.; He, Y.; Chen, Y.; O'Neil, D.; Szymanski, P.; Ei-Sayed, M. A.; Huang, J.; Lin, Z. Meniscus-assisted solution printing of large-grained perovskite films for high-efficiency solar cells. *Nature Communications* **2017,** *8*, 16045, DOI: 10.1038/ncomms16045

https://www.nature.com/articles/ncomms16045#supplementary-information.

(21) Numata, Y.; Kogo, A.; Udagawa, Y.; Kunugita, H.; Ema, K.; Sanehira, Y.; Miyasaka, T. Controlled Crystal Grain Growth in Mixed Cation–Halide Perovskite by Evaporated Solvent Vapor Recycling Method for High Efficiency Solar Cells. *ACS Applied Materials & Interfaces* **2017,** *9* (22), 18739-18747, DOI: 10.1021/acsami.7b02924.

(22) Rau, U. Reciprocity relation between photovoltaic quantum efficiency and electroluminescent emission of solar cells. *Physical Review B* **2007,** *76* (8), 085303, DOI: 10.1103/PhysRevB.76.085303.

(23) Abdi-Jalebi, M.; Andaji-Garmaroudi, Z.; Cacovich, S.; Stavrakas, C.; Philippe, B.; Richter, J. M.; Alsari, M.; Booker, E. P.; Hutter, E. M.; Pearson, A. J.; Lilliu, S.; Savenije, T. J.; Rensmo, H.; Divitini, G.; Ducati, C.; Friend, R. H.; Stranks, S. D. Maximizing and stabilizing luminescence from halide perovskites with potassium passivation. *Nature* **2018,** *555*, 497, DOI: 10.1038/nature25989.

(24) Tuyen, N. T.; Isaac, S.; Gabriella, A.; Diego, C. L.; P., M. P. J.; Aurelio, M. A.; Ivan, M. S. Enhancement of the Performance of Perovskite Solar Cells, LEDs, and Optical Amplifiers by Anti-Solvent Additive Deposition. *Advanced Materials* **2017,** *29* (7), 1604056, DOI: doi:10.1002/adma.201604056.

(25) Momblona, C.; Gil-Escrig, L.; Bandiello, E.; Hutter, E. M.; Sessolo, M.; Lederer, K.; Blochwitz-Nimoth, J.; Bolink, H. J. Efficient vacuum deposited p-i-n and n-i-p perovskite solar cells employing doped charge transport layers. *Energy & Environmental Science* **2016,** *9* (11), 3456-3463, DOI: 10.1039/C6EE02100J.

(26) Ávila, J.; Momblona, C.; Boix, P. P.; Sessolo, M.; Bolink, H. J. Vapor-Deposited Perovskites: The Route to High-Performance Solar Cell Production? *Joule* **2017,** *1* (3), 431-442, DOI: https://doi.org/10.1016/j.joule.2017.07.014.

(27) Wan-Jian, Y.; Tingting, S.; Yanfa, Y. Unique Properties of Halide Perovskites as Possible Origins of the Superior Solar Cell Performance. *Advanced Materials* **2014,** *26* (27), 4653-4658, DOI: doi:10.1002/adma.201306281.

(28) Yin, W.-J.; Shi, T.; Yan, Y. Unusual defect physics in CH3NH3PbI3 perovskite solar cell absorber. *Applied Physics Letters* **2014,** *104*, 063903, DOI: 10.1063/1.4864778.

(29) Li, J. J.; Ma, J. Y.; Ge, Q. Q.; Hu, J. S.; Wang, D.; Wan, L. J. Microscopic Investigation of Grain Boundaries in Organolead Halide Perovskite Solar Cells. *ACS Applied Materials and Interfaces* **2015,** *7* (51), 28518-28523, DOI: 10.1021/acsami.5b09801.

(30) Chu, Z.; Yang, M.; Schulz, P.; Wu, D.; Ma, X.; Seifert, E.; Sun, L.; Li, X.; Zhu, K.; Lai, K. Impact of grain boundaries on efficiency and stability of organic-inorganic trihalide perovskites. *Nature Communications* **2017,** *8* (1), 2230, DOI: 10.1038/s41467-017-02331-4.

(31) Zhao, Y.; Wei, J.; Li, H.; Yan, Y.; Zhou, W.; Yu, D.; Zhao, Q. A polymer scaffold for self-healing perovskite solar cells. *Nature Communications* **2016,** *7*, 10228, DOI: 10.1038/ncomms10228

http://www.nature.com/articles/ncomms10228#supplementary-information.

(32) Manshor, N. A.; Wali, Q.; Wong, K. K.; Muzakir, S. K.; Fakharuddin, A.; Schmidt-Mende, L.; Jose, R. Humidity versus photo-stability of metal halide perovskite films in a polymer matrix. *PCCP* **2016,** *18* (31), 21629-21639.

(33) Yichuan, L.; Yu, T.; Xi, W.; C., W. J.; M., K. J.; Fernando, P. O.; Yijun, D.; Lei, T.; Kenneth, H.; Biwu, M.; Hanwei, G. Enhanced Optical and Electrical Properties of Polymer-Assisted All-Inorganic Perovskites for Light-Emitting Diodes. *Advanced Materials* **2016,** *28* (40), 8983-8989, DOI: doi:10.1002/adma.201602513.

(34) Baodan Zhao; Sai Bai; Vincent Kim; Robin Lamboll; Ravichandran Shivanna, F.; lorian Auras; Johannes M. Richter; Le Yang; Linjie Dai; Mejd Alsari; Xiao-Jian She; Lusheng Liang; Jiangbin Zhang; Samuele Lilliu; Peng Gao; Henry J. Snaith; Jianpu Wang; Neil C. Greenham; Richard H. Friend; Di, D. High-efficiency perovskite-polymer bulk heterostructure light-emitting diodes. *arxiv.org* **2018**, https://arxiv.org/abs/1804.09785, DOI: https://arxiv.org/abs/1804.09785.

(35) Hu, H.; Wong, K.; Kollek, T.; Hanusch, F.; Polarz, S.; Docampo, P.; Schmidt-Mende, L. Highly Efficient Reproducible Perovskite Solar Cells Prepared by Low-Temperature Processing. *Molecules* **2016,** *21* (4), 542.

(36) Pistor, P.; Ruiz, A.; Cabot, A.; Izquierdo-Roca, V. Advanced Raman Spectroscopy of Methylammonium Lead Iodide: Development of a Non-destructive Characterisation Methodology. *Scientific Reports* **2016,** *6*, 35973, DOI: 10.1038/srep35973

https://www.nature.com/articles/srep35973#supplementary-information.

(37) Calabrò, E.; Matteocci, F.; Palma, A. L.; Vesce, L.; Taheri, B.; Carlini, L.; Pis, I.; Nappini, S.; Dagar, J.; Battocchio, C.; Brown, T. M.; Di Carlo, A. Low temperature, solution-processed perovskite solar cells and modules with an aperture area efficiency of 11%. *Solar Energy Materials and Solar Cells* **2018,** *185*, 136-144, DOI: https://doi.org/10.1016/j.solmat.2018.05.001.

(38) Zimmermann E., W. K. K., Müller M., Hu H., Ehrenreich P., Kohlstädt M., Würfel U., Mastroianni S., Mathiazhagan G., Hinsch A, Gujar T.P., Thelakkat M, Pfadler T., Schmidt-Mende, L. Characterization of Perovskite Solar Cells: Towards a Reliable Measurement Protocol. *APL Materials* **2016,** *Under review*, xx, xx.

(39) Oku, T. Crystal Structures of CH3NH3PbI3 and Related Perovskite Compounds Used for Solar Cells. *Solar Cells Leonid A. Kosyachenko, IntechOpen* **2015**, 10.5772/59284, DOI: 10.5772/59284.

(40) DeQuilettes, D. W.; Vorpahl, S. M.; Stranks, S. D.; Nagaoka, H.; Eperon, G. E.; Ziffer, M. E.; Snaith, H. J.; Ginger, D. S. Impact of microstructure on local carrier lifetime in perovskite solar cells. *Science* **2015,** *348* (6235), 683-686, DOI: 10.1126/science.aaa5333.

(41) Wolfgang, T. Perovskite Solar Cells on the Way to Their Radiative Efficiency Limit – Insights Into a Success Story of High Open-Circuit Voltage and Low Recombination. *Advanced Energy Materials* **2017,** *7* (14), 1602358, DOI: doi:10.1002/aenm.201602358.

(42) Ran, C.; Xu, J.; Gao, W.; Huang, C.; Dou, S. Defects in metal triiodide perovskite materials towards high-performance solar cells: origin, impact, characterization, and engineering. *Chemical Society Reviews* **2018**, DOI: 10.1039/C7CS00868F.

(43) Leijtens, T.; Eperon, G. E.; Barker, A. J.; Grancini, G.; Zhang, W.; Ball, J. M.; Kandada, A. R. S.; Snaith, H. J.; Petrozza, A. Carrier trapping and recombination: the role of defect physics in enhancing the open circuit voltage of metal halide perovskite solar cells. *Energy & Environmental Science* **2016,** *9* (11), 3472-3481, DOI: 10.1039/C6EE01729K.

(44) Xing, G.; Mathews, N.; Lim, S. S.; Yantara, N.; Liu, X.; Sabba, D.; Grätzel, M.; Mhaisalkar, S.; Sum, T. C. Low-temperature solution-processed wavelength-tunable perovskites for lasing. *Nature materials* **2014,** *13*, 476-80, DOI: 10.1038/nmat3911.

(45) Li, C.; Zhong, Y.; Luna, C.; Unger, T.; Deichsel, K.; Gräser, A.; Köhler, J.; Köhler, A.; Hildner, R.; Huettner, S. Emission Enhancement and Intermittency in Polycrystalline Organolead Halide Perovskite Films. *Molecules* **2016,** *21* (8), 1081.

(46) Quarti, C.; Grancini, G.; Mosconi, E.; Bruno, P.; Ball, J. M.; Lee, M. M.; Snaith, H. J.; Petrozza, A.; Angelis, F. D. The raman spectrum of the CH3NH3PbI3 hybrid perovskite: Interplay of theory and experiment. *Journal of Physical Chemistry Letters* **2014,** *5* (2), 279-284, DOI: 10.1021/jz402589q.

(47) Sears, W. M.; Klein, M. L.; Morrison, J. A. Polytypism and the vibrational properties of PbI2. *Physical Review B* **1979,** *19* (4), 2305-2313, DOI: 10.1103/PhysRevB.19.2305.

(48) Yun, J. S.; Ho-Baillie, A.; Huang, S.; Woo, S. H.; Heo, Y.; Seidel, J.; Huang, F.; Cheng, Y. B.; Green, M. A. Benefit of grain boundaries in organic-inorganic halide planar perovskite solar cells. *Journal of Physical Chemistry Letters* **2015,** *6* (5), 875-880, DOI: 10.1021/acs.jpclett.5b00182.